Research Article Vol. 61, No. 9 / 20 March 2022 / Applied Optics 2207

applied optics

Performance analysis of a compact auto-phoropter for accessible refractive assessment of the human eye

Farhad Akhoundi,[1,*] Erol Ozgur,[1] Craig Draper,[1,2] Ram Voorakanam,[2] Jaclyn Wycoff,[1,2] Daniel Reetz,[2] Pierre-Alexandre Blanche,[1,2] Lloyd LaComb,[1,2] Gholam Peyman,[1,2] Jim Schwiegerling,[1,2] and N. Peyghambarian[1,2]

[1]Wyant College of Optical Sciences, The University of Arizona, 1630 E University Blvd, Tucson, Arizona 85721, USA
[2]ICRX Inc., 1430 N 6th Ave, Tucson, Arizona 85705, USA
*Corresponding author: akhoundi@optics.arizona.edu

Received 9 November 2021; revised 5 February 2022; accepted 9 February 2022; posted 10 February 2022; published 14 March 2022

We present the performance analysis and specifications of a portable auto-phoropter system that can be employed for fast refractive assessment of a large population. A customized Shack–Hartmann wavefront sensor is developed to accurately measure the defocus and astigmatism of the eye within ±10 D and ±6 D, respectively. Three fluidic lenses are designed to correct the vision in real time. A digital Snellen chart is integrated into the system to validate the accuracy of the measurement and the correction by means of achieving 20/20 vision. The refractive error of eight subjects (16 eyes) has been measured objectively (without patient's feedback) using the proposed system and the results are compared with their clinical prescription through the Bland–Altman method. It is shown that the auto-phoropter takes less than 8 s to measure and correct the eye refractive error with an accuracy of ±0.25 D.

https://doi.org/10.1364/AO.442769

1. INTRODUCTION

Worldwide, approximately one in 12 people suffers from insufficient or no visual correction [1]. About 43% of people with uncorrected vision will eventually become visually impaired [2]. Therefore, regular eye examinations are crucial to addressing global visual impairment. Providing an affordable, accessible, convenient, and fast eye refractive error measurement is a fundamental step to prevent loss of vision for millions of people around the world but in particular within the developing countries.

Unfortunately, subjective refractive error measurement using conventional phoropters with trial lenses is too complex and time-consuming to address the need for improved refractive measurements. In general, too many trial lenses with various dioptric power in both spherical and cylindrical shapes are needed to evaluate the patient's eye refractive error. Liquid lenses which have a tunable dioptric power are a promising alternative to significantly simplify the traditional phoropters [3–8]. Therefore, it is possible to design a compact and portable phoropter based on fluidic lenses.

Traditional phoropters require frequent and reliable feedback from the patients to determine the refractive correction. This may result in confusion and inaccuracy especially for young children, elderly, or mentally handicapped subjects. Therefore, auto-refractors have been used to objectively measure the refractive error. However, since they often provide a rough estimate of the refractive error, their accuracy needs to be validated by an optometrist using trial lenses [9].

In this paper, we propose an instrument which combines a precise auto-refractor based on wavefront sensing technology and a phoropter based on fluidic lenses. Since this device automatically measures the refractive error of the eye and objectively corrects the vision using tunable lenses, we named this device an auto-phoropter [10]. In this device, we have employed a customized Shack–Hartmann (SH) wavefront sensor, which has been used extensively for adaptive optical systems in astronomy [11–13], to measure the human eye's refractive error even in extreme cases (±10 D). It has been shown that the SH sensors are capable of accurate measurement of both lower-order aberration (defocus and astigmatism) of the eye and higher-order aberrations [14–16]. The working principle of the SH sensor is to determine the eye's aberrations based on the measurement of the local slopes of the wavefront reflected off the retina [17,18]. Once the refractive error is measured, the fluid lenses in the system will be activated to correct the patient's vision. A digital Snellen chart will be shown to the subject to confirm that 20/20 vision has been achieved. In some rare cases the patient might not be satisfied with the proposed objective refractive error obtained using the wavefront sensor [19]. We have designed

an optional manual adjustment for the device by which the user/optometrist can fine tune the defocus of the fluid lenses while the patient is looking at the digital Snellen chart. Using the patient feedback, it is then possible to obtain the best subjective refractive error correction. Note that in contrast with the traditional phoropter which requires frequent and reliable intervention from patients, our proposed device will measure and correct the objective refractive error in a few seconds, therefore reducing the feedback required from the subject.

The digital Snellen chart used to verify the patient acuity can easily be changed to display letters, "E" letters with different orientation, or other symbols to address the specific needs of illiterate young children. The details of the design and measurement procedure are presented in the following sections.

2. AUTO-PHOROPTER DESIGN

The proposed system block diagram is presented in Fig. 1. An infrared (IR) LED with 820 nm central wavelength is spatially filtered by an optical fiber and the output of the fiber is collimated using an air-spaced doublet collimator specially designed to deliver a collimated beam with minimal aberration. This wavelength is chosen to maximize the retinal reflection [20]. The LED is faintly visible to the human eye. It is worth mentioning that using an LED instead of a laser reduces the speckle noise on the CMOS sensor and lowers the cost of the system. A polarizer after the collimator makes the beam linearly polarized. The beam diameter is set to 2 mm using an iris after the collimator. The beam is reflected toward the eye-model using a polarizing beam splitter (PBS). The total power of the beam is around 2 μW. We used a custom-built model eye for the initial tests, which is an aspheric 17 mm focal length lens with a diffuse reflector on its back focal plane. An iris in front of the model eye resembles the eye pupil. The IR beam propagating toward the model eye will be focused at the diffused reflector which resembles the retina. The diffusely reflected light can be considered as an unpolarized point source that will be collimated using the eye-model lens. For an ideal model eye this reflected beam is a plane wave; however, for a human eye, it is a distorted wavefront due to the ocular aberrations. Note that in this configuration, the light passes through the optics of the eye twice; however, since the retina can be considered as a diffused reflector, the wave aberrations that are introduced by the eye in the first pass do not affect the measurements [21]. Note also that the residual specular reflection from the retina, which has the same polarization as the incident beam, will be blocked by the PBS.

L1 and L2 construct a one-to-one telescope that relays the eye-model pupil to an intermediate pupil at the fluidic lenses. L3 and L4 construct another one-to-one telescope which relays the intermediate pupil to the SH entrance pupil. Therefore, the wavefront at the exit pupil of the model eye is duplicated at the SH sensor entrance pupil where the local slopes are measured. The iris between L1–L2 is used to block the off-axis corneal reflection from the front surface of the eye-model. Another iris is employed between L3–L4 to reduce stray light reflected from fluid lens surfaces. The L1 and L2 lenses are both achromatic doublets and have a maximum of $\lambda/7$ waves of spherical aberration over the range of −10 D to 10 D. In other words, they are designed to remain diffraction limited in the visible and NIR spectrum.

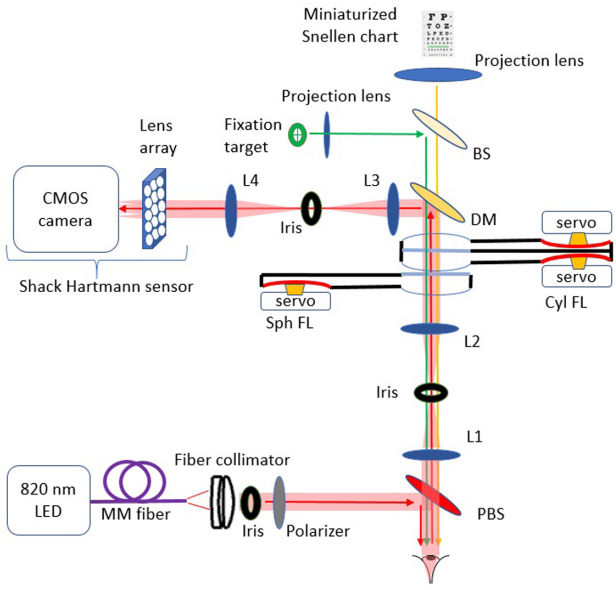

Fig. 1. Block diagram of the proposed auto-phoropter system. The red arrow shows the infrared beam from the 820 nm LED used to measure the refractive error of the eye. The green arrow is the optical path of the fixation target, and the orange arrow shows the beam path of the backlit chrome masked Snellen chart. PBS, polarizing beam splitter; FL, fluidic lens; DM, dichroic mirror.

A. Customized SH Sensor

The SH sensor is an optical metrology tool in which the incoming wavefront is divided into small sub-apertures by means of a microlens array. In the focal plane of the lens array, where a high-resolution CMOS sensor is placed, the system will produce a pattern of spots. By measuring the displacement of each spot from the center of the sub-aperture, the local slope of the wavefront can be estimated. These slopes are then used to reconstruct the wavefront. To calibrate the sensor, a well-collimated beam (plane wave) propagating perpendicular to the lens array is used and the resulting regular spot pattern will be used as the reference for measuring the spot displacement.

In general, the smaller the sub-aperture (lens array pitch) is, the more accurate the wavefront approximation is. However, there are two major limitations in minimizing the lens array pitch. First, the maximum slope that can be measured is proportional to the sub-aperture size. In other words, if we choose a lens array pitch that is too small, for steep slopes, the corresponding spot may fall into the adjacent sub-aperture which causes errors in the slope calculation [22]. Second, the signal-to-noise ratio of the spot pattern is quadratically proportional to the sub-aperture size. Therefore, when measuring a wavefront with very low intensity, the small sub-aperture size will not provide adequately bright spots for analysis.

Another crucial factor for choosing a lens array for the SH sensor is the focal length of the lens array. In general, considering a given CMOS pixel size for imaging, a longer focal length provides more precision in measuring the wavefront local slopes but limits the maximum slope that can be measured. To optimize

Table 1. Zernike Coefficients Relevant to the Defocus and Astigmatism of the Human Eye

Coefficient	Zernike Polynomial	Interpretation
$Z_4(\rho,\theta)$	$\rho^2\sin(2\theta)$	Astigmatism with axis at 45°
$Z_5(\rho,\theta)$	$2\rho^2-1$	Defocus
$Z_6(\rho,\theta)$	$\rho^2\cos(2\theta)$	Astigmatism with axis at 90°

the array lens parameters (pitch and focal length), we simulated Shack–Hartmann wavefront sensors with various pitch and focal length values in Zemax OpticsStudio raytracing software. Then, we observed generated spot patterns from the spherical wavefronts corresponding to a defocused eye-model (±10 D) as well as cylindrical wavefronts corresponding to a range of astigmatic eye-model (± 6 D). The eye-model pupil diameter in the simulation was 3 mm. The optimized lens array parameters which maximize the dynamic range of the system and maintain an acceptable wavefront estimation accuracy (0.01 D) were found. To validate the accuracy of the system, an eye-model with lenses with 0.01 D defocus increments was successfully measured over a range of ±10 D.

In the customized SH sensor, the CMOS sensor exposure time is set so that we can obtain the wavefront error in real time. The generated spot pattern images are analyzed in the software that we developed in-house. First, the beam centroid and diameters are estimated. Then, the centroid of each spot is located and consequently, the local slope of the wavefront is measured by obtaining the spot displacement compared to the reference spot location in each sub-aperture [23]. Then, the wavefront is approximated from the slope measurement using the technique explained in [17]. Therefore, the software provides the Zernike coefficients up to the fourth degree (Z_1 to Z_{15}) corresponding to the reconstructed wavefront. However, only three Zernike coefficients, which are shown in Table 1, are responsible for lower-order aberrations of the eye. These Zernike coefficients can be converted to optometric values (Sph, Cyl, Axis) using the procedure explained in [20]. Although we are not able to correct for higher-order aberrations with the fluidic lenses, the measurements of the high-order Zernike coefficient by the SH sensor are still relevant for other interventions such as Lasik eye surgery. They might also be used to explain why the patient does not achieve 20/20 vision after correction.

B. Fluidic Lens System

The fluidic lens system is constructed from one spherical and two cylindrical fluidic lenses. The axes of the two cylindrical lenses are separated by 45°; therefore, they can be used to correct astigmatism of the eye with any given axis [20,22]. The spherical fluidic lens is responsible for correcting the defocus of the eye. Each fluidic lens is made of a glass substrate, a thin polydimethylsiloxane (PDMS) front membrane, an index matching liquid, and a reservoir [4,6,7,10]. The power of each lens can be tuned by a diaphragm pump mechanism actuated by a servo motor. The step size of the servo motor determines the tuning resolution (~0.01 D) of each fluidic lens. The maximum ranges of dioptric power that can be achieved by the spherical and cylindrical fluidic lenses are ±10 D and ±6 D, which are much greater than other types of tunable lenses such as liquid crystal lenses [24]. Also, compared to deformable mirrors which

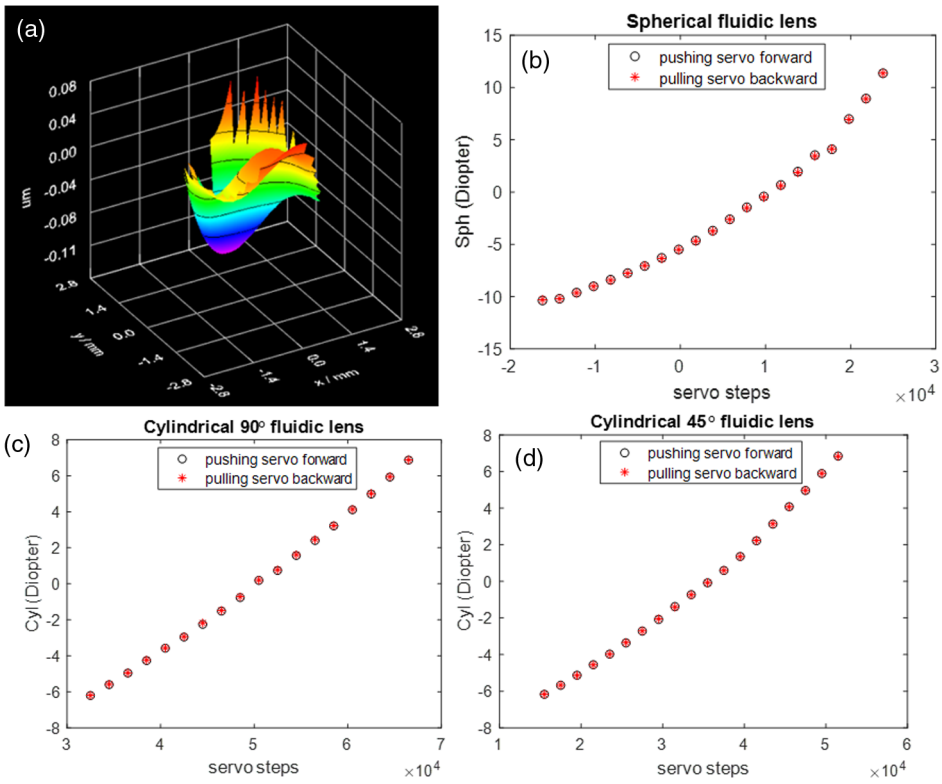

Fig. 2. (a) Accumulated aberrations induced by the PDMS membranes of three fluidic lenses. The peak to valley of the aberration within 3 mm aperture is less than 0.1 μm, which is negligible. (b)–(d) Lens power versus servo motor position for each lens.

are very common in adaptive optics applications, fluidic lenses are significantly less expensive to manufacture. More details on the design of the cylindrical fluid lens are published in [25].

In order to confirm that the PDMS membranes of the fluidic lenses are not degrading the optical performance of the system, we measured the accumulated wavefront errors of the three lenses at flat state (zero diopters), using a commercial wavefront sensor. As shown in Fig. 2(a), the peak to valley of the wavefront error within 3 mm pupil size is about 0.1 um, which allows the entire system to be diffraction limited. It has to be noted that the wavefront error of the fluidic lenses is at its worst in the flat state because the membrane is optically twisted by the support flange of the fluid cavity. Once the membrane is under tension either inflated or deflated, the wavefront will improve.

Figures 2(b)–2(d) show the dioptric power change versus the servo motor position for spherical, 90° cylindrical, and 45° cylindrical fluidic lenses, respectively, measured using our custom SH sensor. Note that, in order to obtain repeatable results from each fluidic lens we need to ensure that there is no hysteresis in the lenses as we push the diaphragm forward or we pull it backward. Note also that the change in the lens power is not necessarily linear. However, the software uses a polynomial curve fitting to obtain the desired dioptric power for each lens.

C. Integrated Snellen Chart and Fixation Target

As mentioned before, to prevent the eye movement and to stabilize the accommodation, a fixation target is employed in the system. A ring-shape target with a crosshair at the center is manufactured using a chrome mask on a silica substrate. A 540 nm LED is used to back illuminate the mask. A lens is used to project the fixation target at 20 ft. The LED can be turned on in the software to fixate the eye during the measurement. The field of view (FOV) of the fixation target is designed to be narrow enough to prevent eye motion.

A similar approach is used to make a digital Snellen chart projected at 20 ft. However, we employed a white LED for back illumination of the chrome mask Snellen chart. This chart is turned on in the software when the measurement and correction is finished so that the accuracy of the measurement and correction of the refractive error can be validated by the subject by means of seeing the 20/20 line of the chart. The FOV of the Snellen chart is designed to be large enough so that it is not sensitive to eye and head motion.

In the case that the subject cannot read well 20/20 line on the chart, we have an optional manual adjustment built in the device by which the operator can tune the fluid lens power. After the objective refractive error is measured and corrected, the optometrist can adjust the correction manually while the patient is looking at the Snellen chart, in order to obtain the best subjective refractive error correction. However, in our human eye measurement study presented in Section 3, all subjects were able to read the 20/20 line after objective refractive error correction. Therefore, we did not need to use this manual adjustment.

To avoid using any flipping mirror in the system, the Snellen chart and fixation target were combined using a beam splitter and they could be turned on and off independently in the software. Since we are using LEDs as a light source for the IR beam, fixation target, and the Snellen chart, the power requirement for the system is very low and the system can be powered by batteries.

Table 2. Comparison of Maximum Corneal and Retinal Exposure of our Device with the Permissible Exposure in ISO-15004-2 Standard

Maximum Irradiance	Threshold for Group 1 Instruments in ISO-15004-2 (at 820 nm)	Auto-Phoropter
On the cornea	20 mW/cm^2	40 $\mu W/cm^2$
On the retina	1.2 W/cm^2	0.34 W/cm^2

D. Light Hazard Measurement

Before performing any measurements on the human eye, we had to confirm that our device was in compliance with ISO-15004-2 standard and therefore is safe to use on the human eyes [26]. Based on Table 2 in this standard, the proposed instrument can be classified in Group 1 if corneal irradiance is less than 20 mW/cm^2 and the retinal irradiance is less than 1.2 W/cm^2 (weighted at 820 nm). In our device, a collimated beam of IR light with a total power of 2 μW is directed toward the eye. This power is uniformly distributed over a 2.5 mm beam diameter. Therefore, the irradiance on the cornea is 40 $\mu W/cm^2$. To determine the maximum exposure on the retina, we simulated the irradiance pattern on the retina surface of the Arizona eye-model [20] in Zemax (Fig. 3). In this model, the output of the fiber is collimated and reflected toward the eye-model. As shown in Fig. 3(b), the peak irradiance on the retina surface is 0.34 W/cm^2. Note that if the eye has some refractive error, the peak irradiance on the retina will decrease to a lower value. For instance, in Fig. 2(c), the irradiance on the retina for the Arizona eye-model with 0.5 D defocus has been shown. Therefore, based on these exposure values, the proposed auto-phoropter can be classified as a Group 1 ophthalmic device for which no potential light hazard exists [27].

3. HUMAN EYE REFRACTIVE ERROR MEASUREMENT

To demonstrate the performance of the proposed auto-phoropter on the human eye, we performed measurement on 16 eyes (eight subjects). The measurement was done according to a protocol approved by the Institutional Review Boards at the University of Arizona. The subjects' ages ranged from 22 to 50 years old and their eyes were either myopic and/or astigmatic. The mean and standard deviation (STD) of the volunteers' spherical refractive error are −1.97 D and 1.42 D, respectively. The mean and STD of volunteers' cylindrical aberration are −0.75 D and 0.48 D, respectively. In the experiment, the subjects were asked to look at the fixation target to stabilize the accommodation and fixate their eye position. A chin rest was used to stabilize the subject's head. By observing the spot pattern at the SH sensor, the operator can guide the subject to align his/her eye with the optical axis of the device. Note that before the measurement, the fluidic lenses are set at zero position (flat state).

Once the subject's eye is at the correct position and he/she can see the fixation target, the IR wavefront reflected off the retina

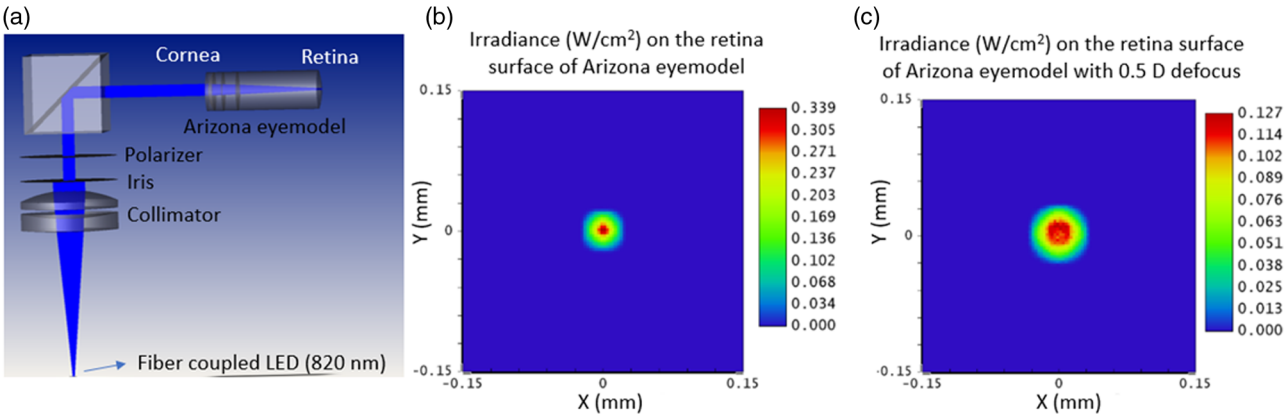

Fig. 3. (a) Zemax model used to simulate the retinal irradiance pattern. (b) Irradiance pattern on the retina surface of the Arizona eye-model. (c) Retinal irradiance pattern of the Arizona eye-model with 0.5 D defocus.

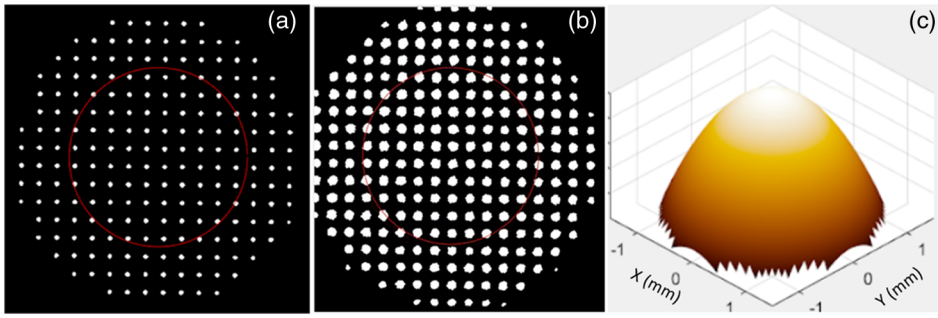

Fig. 4. (a) Spot pattern on the SH sensor for a house-made eye-model, which is used for calibration. (b) Spot pattern corresponding to a myopic eye with 4 D defocus. (c) Reconstructed wavefront error from the spot pattern in (b).

will appear in real time in the software (Fig. 4). Then, the operator will click the "measure and correct" button in the software to start the measurement. The software calculates the refractive error of the eye from the estimated Zernike coefficients. Note that the wavefront aberration is measured over 3 mm pupil diameter to exclude the effect of higher-order aberration of the eye. The natural pupil diameter of the subjects' eye in this study is larger than 3 mm during measurement in a dimmed light condition. Therefore, we do not need to use any drug to dilate the pupil.

In Fig. 4(a), the spot pattern from the house-made eye-model which is used for calibration is shown. The spot pattern and the reconstructed wavefront for a subject's eye with 4 D myopic vision is also shown in Figs. 4(b) and 4(c).

The software then sends commands to the fluid lens system to correct for the measured refractive error. The astigmatism is corrected using the cylindrical lenses and the defocus is corrected using the spherical lens. After correction, which takes about 3 s, the digital Snellen chart which is virtually projected at 20 feet is shown to the subject to validate the refractive error measurement. Confirmation of the visual acuity is obtained by asking the subject to read the 20/20 line of the chart.

To evaluate the accuracy of the prescription provided by the proposed auto-phoropter, we compared the measured prescription of the eight subjects (16 eyes) with their recent clinical

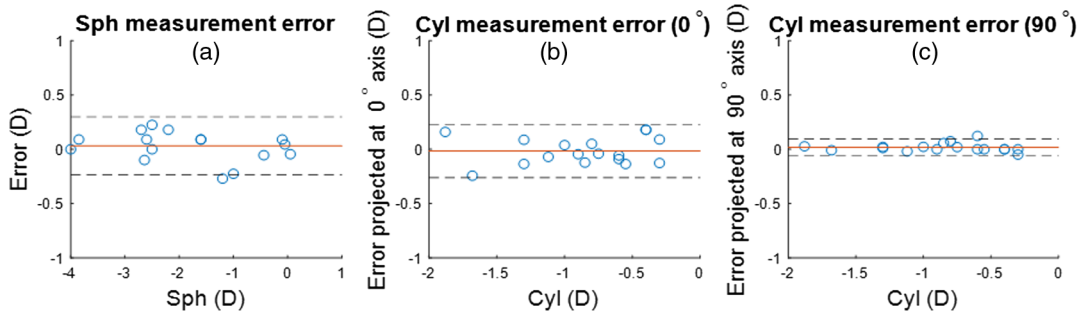

Fig. 5. Difference (error) between the proposed device measurement and clinical prescription for eight subjects (16 eyes). (a) Difference in spherical values. (b), (c) Difference in cylindrical values projected at 0 and 90 deg axis. Red solid line is the error mean, and dashed lines are limits of agreement.

prescription. As shown in Figs. 5(a)–5(c), the Bland–Altman method [28] is used to show that the error in the measured astigmatism and defocus is within ±0.25 D. We observed that the auto-phoropter measures the axis of the astigmatism with less than 10° error. All subjects were able to read the 20/20 line of the Snellen chart after the proposed correction was applied to the fluidic lenses. The errors introduced by the system have been minimized to achieve a measurement accuracy of ±0.01D at the SH sensor, and ±0.1 D reproducible by the fluidic lens. One source of error observed in Fig. 5 is from the clinical prescription values that are measured to the nearest quarter diopter (±0.25 D) using trial lenses. To the best of our knowledge, our instrument outperforms the conventional phoropter equipment used by optometrists. Note that the purpose of this study is to demonstrate the concept of the proposed system. A separate study with a larger population of subjects and with wider range of myopic, hyperopic, and astigmatic eyes is ongoing which will be published elsewhere.

4. CONCLUSION

We demonstrate the design, implementation, and performance analysis of an accessible auto-phoropter. The compact design of the device ($30 \times 30 \times 30$ cm^3) makes it portable. Customized components such as a Shack–Hartmann sensor and a fluidic lens system were developed to accurately measure and correct the refractive error of the human eye. Since the measurement is objective and patient's feedback is not required, it can be used to assess the visual acuity of young children, elderly, or mentally handicapped. It was discussed that the proposed device can measure and correct the human eye in less than 8 s which makes it attractive for screening a large population of subjects such as in schools. Based on measurements on 16 eyes, the prescription provided by the auto-phoropter is consistent with the clinical prescription with less than 0.25 D error. For next steps, we are working on the binocular version of the device as well as testing the device on a larger and more diverse population.

Funding. State of Arizona TRIF Photonics.

Disclosures. FA, CD, RV, JW, DR, PAB, LL, GP, JS, NP: ICRX Inc. (E, I).

Data availability. Data underlying the results presented in this paper are not publicly available at this time but may be obtained from the authors upon reasonable request.

REFERENCES

1. T. Vos, A. A. Abajobir, K. H. Abate, C. Abbafati, K. M. Abbas, F. Abd-Allah, R. S. Abdulkader, A. M. Abdulle, T. A. Abebo, and S. F. Abera, "Global, regional, and national incidence, prevalence, and years lived with disability for 328 diseases and injuries for 195 countries, 1990–2016: a systematic analysis for the Global Burden of Disease Study 2016," Lancet **390**, 1211–1259 (2017).
2. World Health Organization, "Visual impairment and blindness," 2014, http://www.who.int/mediacentre/factsheets/fs282/en/.
3. G. A. Peyman, "External lens adapted to change refractive properties," U.S. patent US20070142909A1 (09 August 2011).
4. R. Marks, D. L. Mathine, G. Peyman, J. Schwiegerling, and N. Peyghambarian, "Adjustable fluidic lenses for ophthalmic corrections," Opt. Lett. **34**, 515–517 (2009).
5. G. A. Peyman, N. N. Peyghambariam, and R. L. Marks, "External lens with flexible membranes for automatic correction of the refractive errors of a person," U.S. patent US8409278B2 (2 April 2013).
6. K. Wei, H. Huang, Q. Wang, and Y. Zhao, "Focus-tunable liquid lens with an aspherical membrane for improved central and peripheral resolutions at high diopters," Opt. Express **24**, 3929–3939 (2016).
7. H. Ren, D. Fox, P. A. Anderson, B. Wu, and S.-T. Wu, "Tunable-focus liquid lens controlled using a servo motor," Opt. Express **14**, 8031–8036 (2006).
8. D. Kopp and H. Zappe, "Tubular astigmatism-tunable fluidic lens," Opt. Lett. **41**, 2735–2738 (2016).
9. K. Pesudovs and H. S. Weisinger, "A comparison of autorefractor performance," Optom. Vis. Sci. **81**, 554–558 (2004).
10. B. Amirsolaimani, G. Peyman, J. Schwiegerling, A. Bablumyan, and N. Peyghambarian, "A new low-cost, compact, auto-phoropter for refractive assessment in developing countries," Sci. Rep. **7**, 13990 (2017).
11. B. Platt and R. V. Shack, "Lenticular Hartmann screen," Opt. Sci. Newsl. (Univ. Ariz.) **5**, 15 (1971).
12. J. W. Goodman, *International Trends in Optics* (Academic, 2012).
13. R. Shannon, *Applied Optics and Optical Engineering* (Elsevier, 2012), Vol. **8**.
14. J. Liang, D. R. Williams, and D. T. Miller, "Supernormal vision and high-resolution retinal imaging through adaptive optics," J. Opt. Soc. Am. A **14**, 2884–2892 (1997).
15. M. Salas, W. Drexler, X. Levecq, B. Lamory, M. Ritter, S. Prager, J. Hafner, U. Schmidt-Erfurth, and M. Pircher, "Multi-modal adaptive optics system including fundus photography and optical coherence tomography for the clinical setting," Biomed. Opt. Express **7**, 1783–1796 (2016).
16. M. Rubio, C. S. Hernández, E. Seco, P. Perez-Merino, I. Casares, S. R. Dave, D. Lim, N. J. Durr, and E. Lage, "Validation of an affordable handheld wavefront autorefractor," Optom. Vis. Sci. **96**, 726–732 (2019).
17. W. H. Southwell, "Wave-front estimation from wave-front slope measurements," J. Opt. Soc. Am. **70**, 998–1006 (1980).
18. K. J. Ciuffreda and M. Rosenfield, "Evaluation of the SVOne: a handheld, smartphone-based autorefractor," Optom. Vis. Sci. **92**, 1133 (2015).
19. L. Hervella, E. A. Villegas, P. M. Prieto, and P. Artal, "Assessment of subjective refraction with a clinical adaptive optics visual simulator," J. Cataract Refractive Surg. **45**, 87–93 (2019).
20. J. E. Sheedy, *Field Guide to Visual and Ophthalmic Optics* (SPIE, 2005).
21. F. W. Campbell and R. W. Gubisch, "Optical quality of the human eye," J. Physiol. **186**, 558–578 (1966).
22. J. C. Wyant and K. Creath, "Basic wavefront aberration theory for optical metrology," in *Applied Optics and Optical Engineering* (Academic Press, 1992), Vol. **11**, pp. 28–39.
23. J. Liang, B. Grimm, S. Goelz, and J. F. Bille, "Objective measurement of wave aberrations of the human eye with the use of a Hartmann–Shack wave-front sensor," J. Opt. Soc. Am. A **11**, 1949–1957 (1994).
24. S. Petsch, A. Grewe, L. Köbele, S. Sinzinger, and H. Zappe, "Ultrathin Alvarez lens system actuated by artificial muscles," Appl. Opt. **55**, 2718–2723 (2016).
25. E. Ozgur, D. Reetz, F. Akhoundi, N. O'Brien, J. Wycoff, R. Voorakaranam, P.-A. Blanche, L. LaComb, C. Liang, G. Peyman, and N. Peyghambarian, "Parametric dog-bone-shaped tunable cylindrical fluidic lens," Appl. Opt. **60**, 4755–4761 (2021).
26. I. S. Organization, Ophthalmic Instruments — Fundamental Requirements and Test Methods — Part 2: Light Hazard Protection ISO 15004-2:2007.
27. R. J. Landry, R. G. Bostrom, S. A. Miller, D. Shi, and D. H. Sliney, "Retinal phototoxicity: a review of standard methodology for evaluating retinal optical radiation hazards," Health Phys. **100**, 417–434 (2011).
28. J. M. Bland and D. Altman, "Statistical methods for assessing agreement between two methods of clinical measurement," Lancet **327**, 307–310 (1986).